# Diffractive imaging using a polychromatic high-harmonic generation soft-x-ray source

Ruben A. Dilanian,[1,a)] Bo Chen,[1] Garth J. Williams,[1] Harry M. Quiney,[1] Keith A. Nugent,[1] Sven Teichmann,[2] Peter Hannaford,[2] Lap V. Dao,[2] and Andrew G. Peele[3]
[1]*ARC Centre of Excellence for Coherent X-ray Science, School of Physics, The University of Melbourne, Victoria 3010, Australia*
[2]*ARC Centre of Excellence for Coherent X-ray Science and Centre for Atom Optics and Ultrafast Spectroscopy, Faculty of Engineering and Industrial Sciences, Swinburne University of Technology, Victoria 3122, Australia*
[3]*Department of Physics, ARC Centre of Excellence for Coherent X-ray Science, La Trobe University, Bundoora, Victoria 3086, Australia*

(Received 2 March 2009; accepted 19 June 2009; published online 27 July 2009)

A new approach to diffractive imaging using polychromatic diffraction data is described. The method is tested using simulated and experimental data and is shown to yield high-quality reconstructions. Diffraction data produced using a high-harmonic generation source are considered explicitly here. The formalism can be readily adapted, however, to any short-wavelength source producing a discrete spectrum and possessing sufficient spatial coherence. © *2009 American Institute of Physics*. [DOI: 10.1063/1.3176976]

## I. INTRODUCTION

Coherent diffractive imaging (CDI) is a well-established technique that enables the structure, shape, and size of finite, nonperiodic objects to be deduced from x-ray diffraction intensity measurements.[1–7] In recent years, CDI has been applied successfully to a range of objects, including both inorganic and biological samples.[5–7] The CDI reconstruction technique is based on Fienup's extensions of the algorithm first proposed by Gerchberg and Saxton.[8,9] The Gerchberg–Saxton–Fienup (GSF) algorithm propagates a numerical representation of a scalar wavefield between "object" and "detector" planes using instances of the fast-Fourier transformation. The wavefield in these fixed planes is constrained by the application of *a priori* information, and the iteration between planes is continued until self-consistency is achieved.[9] The reliance on Fourier representations of a single scalar wavefield to carry all of the information about the target system leads to one of the most critical limitations of the GSF approach: the incident beam that illuminates the object must be essentially completely spatially coherent and quasimonochromatic.[2]

The steadily growing demand for high-resolution imaging of the structure and dynamics of weakly scattering, nanoscale objects has driven the development of new x-ray sources. These include free-electron x-ray laser[10] (XFEL) and high-harmonic generation (HHG) sources,[11] both of which exhibit a high degree of spatial coherence but produce an output with multiple longitudinal modes. The extraction of a segment of the spectrum using a narrow-band spectral filter or a monochromator in CDI experiments leads to a significant decrease in the flux of the beam incident on the sample. If a HHG source is employed, such long exposure times may be required that the approach is rendered impractical. In order to make the greatest benefit from the emerging range of intense x-ray sources in CDI experiments, it is desirable that reconstruction methods be developed that are not critically reliant on essentially perfect spatial and temporal coherences.

We have identified two distinct approaches to overcome these difficulties, which are sketched in Fig. 1. The first approach extends the conventional CDI algorithm to enable diffractive imaging to be achieved using polychromatic diffraction data: the *multiwavelength CDI* approach. In a recent publication[12] we demonstrated the ability of this method to reconstruct high-quality images from experimentally collected polychromatic data. In the present article we consider a second, alternative approach. The *two-step CDI* approach is presented in which a single monochromatic component is extracted from polychromatic data enabling the conventional CDI approach to be applied without modification. We here analyze diffraction data produced using a laser-driven HHG source. The formalism applies equally, however, to any short-wavelength source for which there is a high degree of spatial coherence at each sampled wavelength, but poor temporal coherence across the sampled spectrum. The analysis

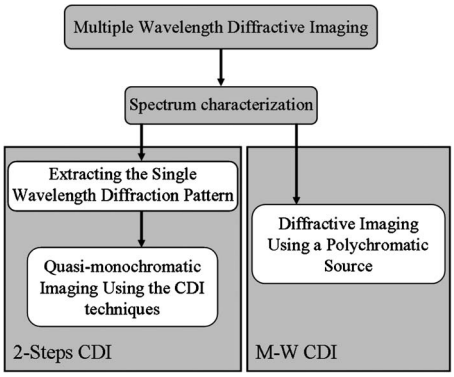


FIG. 1. Schematic of two approaches for the diffractive imaging from polychromatic data.

[a)]Electronic mail: roubend@unimelb.edu.au.

 © 2009 American Institute of Physics

Downloaded 23 Oct 2009 to 136.186.1.189. Redistribution subject to AIP license or copyright; see http://jap.aip.org/jap/copyright.jsp

may also, consequentially, be applied to the multimode XFEL sources that are under current development.

We begin, in Sec. II, with a preliminary analysis of the current limitations of both approaches. The brief reviews of the multiwavelength CDI approach and the detailed description of the two-step CDI approach are presented in Secs. III A and III B, respectively. Section IV provides several examples of reconstruction based on the two-step CDI approach.

## II. INITIAL CONDITIONS AND VALIDITY OF THE MODEL

We consider the formation of diffraction patterns by sources that produce an output with a finite number of discrete longitudinal modes, corresponding, for example, to the harmonics produced by a HHG source. We also assume that there is negligible interference between each frequency component of the spectrum. This is a good approximation for exposure times which are long compared to the beat time between adjacent modes. In this case the total observed intensity distribution of the diffraction pattern, $I_T(\mathbf{R})$, at the position $\mathbf{R}=(X,Y)$ on the detector plane can be represented as the superposition of the intensity distributions $I(\mathbf{R}|\lambda)$ from each mode, so that in discrete form

$$I_T(\mathbf{R}) = \sum_{k=1}^{M} F(\lambda_k) \cdot I(\mathbf{R}|\lambda_k), \tag{1}$$

where the spectrum is considered over the interval $\lambda_C - \Delta\lambda M/2 \le \lambda_k \le \lambda_C + \Delta\lambda M/2$, $M$ is the total number of sample points in the spectrum, and $\lambda_C$ is the wavelength of the central mode. Both approaches assume that the spectrum $F(\lambda)$ of the incident polychromatic illumination is known.[13]

The CDI technique is based on the GSF algorithm which involves iterative forward and back propagations of the complex wavefield between two parallel planes using Fresnel free-space approximation.[14] This corresponds to the condition that the reconstructed image is a projection along the optical axis of the three dimensional; the properties of Fresnel propagation can be used to estimate the tolerable thickness $t$ for which this condition is acceptable,[15]

$$t < \Delta^2/\lambda, \tag{2}$$

where $\Delta$ is the resolution of the reconstruction and $\lambda$ is the wavelength. For example, for the spectrum considered over the interval, 20 nm $<\lambda<$ 45 nm, the thickness of the object must be less then 110 nm for the resolution $\Delta=70$ nm.

It should also be noted that the diffraction pattern should satisfy the oversampling criterion[16] and that the finite size of the object is critical to our ability to obtain a reliable image reconstruction.

## III. POLYCHROMATIC DIFFRACTIVE IMAGING: ALGORITHMS

Although the multiwavelength CDI approach has been covered previously,[12] it is useful to summarize briefly its main features for completeness of the presentation and for comparison with two-step CDI.

### A. Multiwavelength CDI approach

The multiwavelength CDI approach involves a modified iterative reconstruction algorithm that simultaneously uses multiple wavelengths to reconstruct an object consisting of a single known material with complex refractive index $n(\lambda)$. The exit wavefield $\Psi(\mathbf{R}_O|\lambda_k)$ leaving an object illuminated with a coherent plane wave with wavelength $\lambda_k$ can be written in terms of the thickness function $T(\mathbf{R}_O)$,[17]

$$\Psi(\mathbf{R}_O|\lambda_k) = \exp\left[ i\frac{2\pi}{\lambda_k} n(\lambda_k) T(\mathbf{R}_O) \right], \tag{3}$$

where $\mathbf{R}_O$ is the position vector at the object plane. For each single wavelength $\lambda_k$, the propagation of $\Psi(\mathbf{R}_O|\lambda_k)$ to the detector plane, $\Psi(\mathbf{R}_D|\lambda_k)$, can be described using the Fresnel free-space approximation,[14]

$$\Psi(\mathbf{R}_D|\lambda_k) \sim \frac{i}{\lambda_k Z} \hat{F}\left\{ \exp\left( i\pi \frac{R_O^2}{\lambda_k Z} \right) \Psi(\mathbf{R}_O|\lambda_k) \right\}, \tag{4}$$

where $\mathbf{R}_D$ is the position vector at the detector plane, $\hat{F}$ denotes the Fourier transform operator, and $Z$ is the object-detector distance. For the multiwavelength illumination, the observed intensity distribution is the incoherent superposition of $|\Psi(\mathbf{R}_D|\lambda_k)|^2$ from each mode of the spectrum $F(\lambda_k)$ [see Eq. (1)]. The core idea of the multiwavelength CDI approach is to reconstruct the wavelength-independent thickness function $T(\mathbf{R}_O)$. In this case, any mode can be used to satisfy the support constraint at the object plane but we typically choose the most central mode in the wavelength spectrum $\Psi(\mathbf{R}_O|\lambda_C)$. The single back-propagation mode is used as the basis for the update of $T(\mathbf{R}_O)$ and to recalculate $\Psi(\mathbf{R}_O|\lambda_k)$ for all modes, Eq. (4). Therefore, the key extension in this algorithm is the use of multiple forward-propagation modes, $\Psi(\mathbf{R}_O|\lambda_{1\ldots M}) \overset{\mathrm{FP}}{\rightarrow} \Psi(\mathbf{R}_D|\lambda_{1\cdots M})$, combined with a single back-propagation mode, $\Psi(\mathbf{R}_O|\lambda_C) \overset{\mathrm{BP}}{\leftarrow} \Psi(\mathbf{R}_D|\lambda_C)$, during the reconstruction process. In the general case, when the object is not completely opaque to the incident light, the spectral distribution $F(\lambda)$ is modified due to the wavelength-dependent absorption of the sample. To take this into account the values of $F(\lambda)$ are reoptimized during the iterative procedure.

The analysis of the multiwavelength CDI approach shows that the initial guess of the thickness distribution plays an important role in the reconstruction process. We found, for example, that using the autocorrelation function as the initial guess, rather than a uniform distribution, leads to a faster convergence.

### B. Two-step CDI approach

The new approach outlined in the present section consists of two independent parts. Since the second step is common to conventional CDI,[1–7] we consider only the first step in which a single monochromatic component is extracted from polychromatic intensity data. To achieve this let us consider the issue of the diffractive imaging, that is, generally speaking, a two-dimensional (2D) inverse problem embedded in a three-dimensional (3D) coordinate system $\{\mathbf{R},\lambda\}$.

Downloaded 23 Oct 2009 to 136.186.1.189. Redistribution subject to AIP license or copyright; see http://jap.aip.org/jap/copyright.jsp

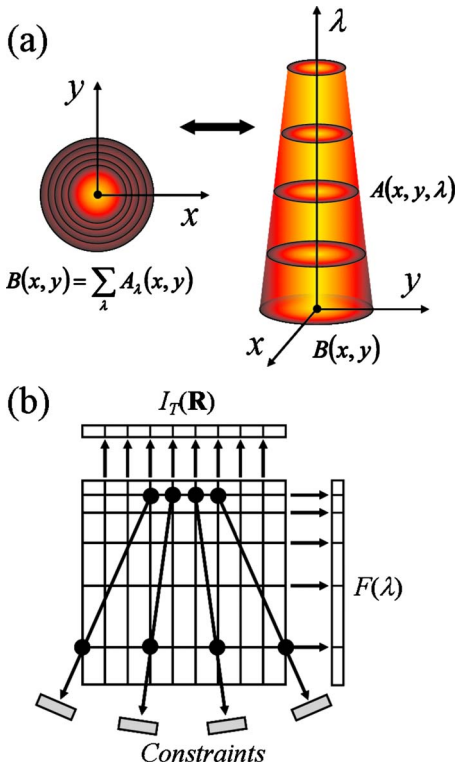


FIG. 2. (Color online) (a) Schematic of the $2D \rightarrow 3D$ transformation for the two-step CDI algorithm. (b) Schematic of the multiprojection ART.

Figure 2(a) schematically shows such a $2D \rightarrow 3D$ transformation. The 2D intensity distribution $I_T(\mathbf{R})$ can be expressed as a projection of the 3D distribution, $I(\mathbf{R},\lambda)=F(\lambda)\cdot I(\mathbf{R}|\lambda)$, and any slice of $I(\mathbf{R},\lambda)$ in the plane $\{\mathbf{R},\lambda_k\}$ is a single component of polychromatic data.

We reconstruct $I(\mathbf{R},\lambda)$ using an algorithm based on the algebraic reconstruction technique (ART),[18,19] which has been developed to reconstruct an image from multiple projection data. In our case there are two types of such projections, schematically represented in Fig. 2(b).

(1) The sum of all intensities $I(\mathbf{R},\lambda)$ at the position $\mathbf{R}$ along the $\lambda$ direction corresponds to the total intensity distribution,

$$I_T(\mathbf{R}) = \sum_{k=1}^{M} I(\mathbf{R},\lambda_k). \tag{5a}$$

(2) The sum of all intensities at a fixed wavelength, $\lambda=\lambda_k$, corresponds to the spectral intensity,

$$F(\lambda) = \sum_{\mathbf{R}} I(\mathbf{R},\lambda). \tag{5b}$$

It is clear that two projections are not sufficient to ensure a unique reconstruction of the $I(\mathbf{R},\lambda)$ function. The scaling properties of $I(\mathbf{R},\lambda)$ provide several additional constraints,[14]

$$I(\mathbf{R},\lambda_k)\cdot\frac{1}{F(\lambda_k)} = \frac{1}{\alpha_{k,k+1}^2} I\left(\frac{\mathbf{R}}{\alpha_{k,k+1}},\lambda_{k+1}\right)\cdot\frac{1}{F(\lambda_{k+1})}, \tag{6a}$$

where $k=1,2,\ldots, M-1$, and $\alpha_{k,k+1}=\lambda_k/\lambda_{k+1}$ is the scaling parameter. The scaling relationship should be applied recursively for every two nearest spectral modes, $F(\lambda_k)$ and $F(\lambda_{k+1})$, started from the shortest wavelength. Here, we assume that the wavelength dependence of the complex refractive index of the object, $n(\lambda)$, can be neglected over the interval $\lambda_k \le \lambda \le \lambda_{k+1}$. This assumption is generally correct for wavelengths sufficiently far from absorption thresholds. Therefore, the algorithm can be applied to binary, real, or complex objects. Equation (6a) can be further simplified if the wavelength dependence of $n(\lambda)$ can be neglected over the interval $\lambda_{\min} \le \lambda \le \lambda_{\max}$ of the spectrum,

$$I(\mathbf{R},\lambda_k)\cdot\frac{1}{F(\lambda_k)} = \frac{1}{\alpha_k^2} I\left(\frac{\mathbf{R}}{\alpha_k},\lambda_C\right)\cdot\frac{1}{F(\lambda_C)}. \tag{6b}$$

In this case, $\alpha_k=\lambda_k/\lambda_C$, where $\lambda_C$ is the central wavelength.

The normalized intensity distribution of the single component of polychromatic data for $\lambda=\lambda_C$ is reached through iterations $l=0,1,2,\ldots$ defined by the additive ART (AART) algorithm,[20]

$$I(\mathbf{R},\lambda)^{(l+1)} = I(\mathbf{R},\lambda)^{(l)} + \eta\left\{\frac{I_T(\mathbf{R}) - I_T^E(\mathbf{R})}{N} + \frac{F(\lambda) - F^E(\lambda)}{M}\right\}, \tag{7}$$

where $I_T^E(\mathbf{R})$ and $F^E(\lambda)$ are normalized measured diffractive intensities and the source spectrum, respectively. The discrepancy between the measured and calculated projection elements is analyzed using

$$\Omega = 0.5\cdot\sqrt{\frac{1}{N}\sum_{\mathbf{R}}[I_T(\mathbf{R}) - I_T^E(\mathbf{R})]^2 + \frac{1}{M}\sum_{\lambda}[F(\lambda) - F^E(\lambda)]^2}. \tag{8}$$

The disadvantage of the AART algorithm is that it leaves artifacts in the reconstructed field.[19] To avoid this behavior the multiplicative ART (MART) algorithm[21] is applied after several iterations of AART,

$$I(\mathbf{R},\lambda)^{(l+1)} = I(\mathbf{R},\lambda)^{(l)}\cdot\left\{\frac{I_T^E(\mathbf{R})}{I_T(\mathbf{R})} + \frac{F(\lambda)}{F(\lambda)}\right\}^{\mu}, \tag{9}$$

where $\mu$ is a relaxation parameter typically chosen to have a value between 0 and 2.

It should be noted that the quality of the CDI reconstruction from extracted single component data depends on the accuracy of the AART/MART reconstruction which, in turn, depends on the accuracy of the different projection calculations, Eq. (5) and (6). The accuracy of the calculation of $I_T(\mathbf{R})$ depends on the signal-to-noise ratio of the intensity distribution measured by the detector and is limited by the resolution of the detector, $\Delta_D$. The accuracy of the $F(\lambda)$ calculation depends on the accuracy of the source spectrum measurement, $\Delta\lambda/\lambda$. The accuracy of the scaling operation, Eq. (6a) or Eq. (6b), can be estimated by considering two spatial positions at the detector plane, $R_1=R$ and $R_2=R/\alpha$. Since $\alpha=\lambda_1/\lambda_2$ and $\Delta R=|R_2-R_1|>\Delta_D$ then $\delta\lambda/\lambda>\Delta_D/R$, where $\delta\lambda=|\lambda_1-\lambda_2|$.

Naturally, the single component corresponding to the shortest wavelength should be used in the CDI reconstruc-

Downloaded 23 Oct 2009 to 136.186.1.189. Redistribution subject to AIP license or copyright; see http://jap.aip.org/jap/copyright.jsp

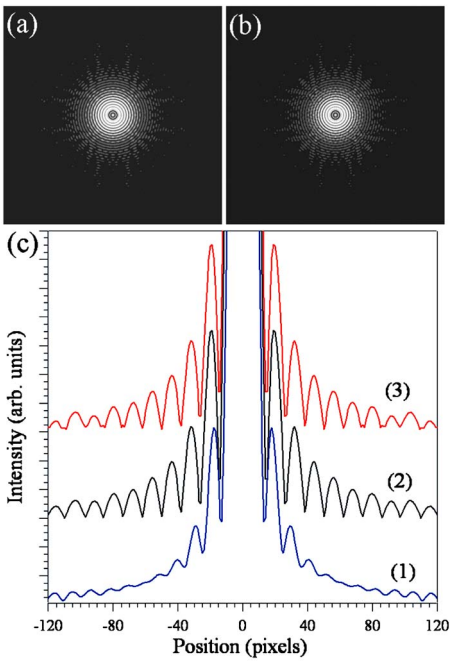


FIG. 3. (Color online) Simulated (a) and reconstructed (b) single component of the polychromatic data obtained from the ideal pinhole. (c) The one-dimensional cross sections of polychromatic (1), simulated monochromatic (2), and reconstructed monochromatic (3) diffraction data.

tion to provide the best possible resolution of the reconstruction. In practice, however, the resolution achievable in the reconstruction is actually limited by the most intense part of the spectrum.[22] The resolution for each mode of the spectrum $\Delta_k$ can be defined as $\Delta_k = 1.22 \cdot \lambda_k / \mathrm{NA}$ (Rayleigh criterion), where NA is the numerical aperture.[17] The effective resolution can then be written in the form $\Delta_E = 1.22 \cdot \Sigma_{k=1}^{M} w_k \cdot \lambda_k / (\mathrm{NA} \cdot M)$ or $\Delta_E = 1.22 \cdot \lambda_E / \mathrm{NA}$, where $w_k = F(\lambda_k) / \max\{F(\lambda)\}$ are the normalized spectral weightings, $\max\{y\}$ denotes the maximum of $y$, and $\lambda_E = \Sigma_{k=1}^{M} w_k \cdot \lambda_k / M$ is the effective wavelength of the spectrum. The value of $\lambda_E$ corresponds to the center of the gravity of the spectrum, which is close to the central peak wavelength in the case of the HHG source.

## IV. RECONSTRUCTION EXAMPLES

*Example 1.* (Fig. 3) The algorithm which extracts a single component of the polychromatic diffraction data was first tested with a 20 $\mu$m pinhole. We assumed 20 $\mu$m resolution at the detector plane and $Z = 100$ mm sample-detector distance. Two diffraction patterns were simulated: a polychromatic pattern using the six wavelengths given in Table I and a monochromatic pattern generated by a single wavelength, $\lambda_C = 32.514$ nm. For each of the six wavelengths we computed $1300 \times 1300$ dimensional monochromatic diffraction patterns, $I(\mathbf{R}|\lambda)$, and combined them using Eq. (1) to obtain the total intensity distribution $I_T(\mathbf{R})$. A single component was then isolated from the polychromatic data. Simulated and reconstructed single wavelength diffraction patterns are shown, respectively, in Figs. 3(a) and 3(b); they are barely distinguishable. Figure 3(c) shows the one-dimensional cross sections of polychromatic (1), simulated (2), and reconstructed (3) data for the purpose of better comparison. It can be seen that the reconstructed pattern is in good agreement with the original simulated example.

TABLE I. Simulated spectral distribution $F(\lambda)$.

| $\lambda$ (nm) | $F(\lambda)$ |
|---|---|
| 27.806 | 0.24 |
| 29.960 | 0.40 |
| 32.514 | 1.00 |
| 35.546 | 0.77 |
| 38.978 | 0.22 |
| 43.207 | 0.10 |

*Example 2.* (Fig. 4) In this case we analyzed data obtained from a simulated 20 $\mu$m pinhole with a vertical bar inside its boundary. The same conditions were used to simulate polychromatic diffraction data, and the two-step CDI algorithm was applied to reconstruct the object. We first extracted the single component of polychromatic data. Figures 4(a) and 4(b) represent the simulated and reconstructed single wavelength diffraction patterns, respectively. We then reconstructed the image of the object using the conventional CDI approach. The simulated object is shown in Fig. 4(c). The resulting reconstruction is shown in Fig. 4(d) which used the support indicated by the dashed rectangle shown.

*Example 3.* (Fig. 5) This example demonstrates the effectiveness of the image reconstruction from experimental data collected using a HHG soft-x-ray source.[23] We used the two-step CDI approach to reconstruct the image of the 25 $\mu$m pinhole, Fig. 5(a). As seen from the Fig. 5(a), the object has a strongly pronounced defect structure that significantly changes the diffraction pattern. In the experimental setup we used 29 fs laser pulses generated by a 1 kHz amplified Ti:sapphire laser system, which operates at a central wavelength of 810 nm. The pulse is focused inside a semi-infinite argon gas cell by means of a 0.5 m focal length lens. The cell is operated at a pressure of 20 torr. The harmonic beam, which is comprised of several harmonic components, is separated from the fundamental beam by 0.2 $\mu$m thick Al

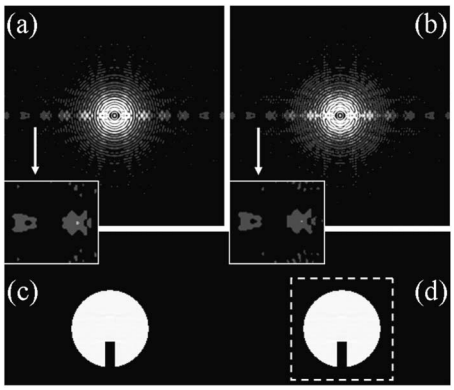


FIG. 4. (a) Simulated monochromatic diffraction intensities. (b) The single component of the diffraction pattern reconstructed from simulated polychromatic data. (c) Original image of the object. (d) Output of the two-step CDI iterative scheme. The dashed rectangle indicates the support assumed in the reconstruction.

Downloaded 23 Oct 2009 to 136.186.1.189. Redistribution subject to AIP license or copyright; see http://jap.aip.org/jap/copyright.jsp

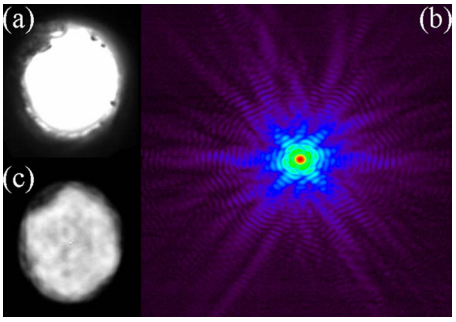


FIG. 5. (Color online) (a) An optical microscope image of the sample used in the diffraction experiment. (b) Diffraction data acquired from the sample. The data are displayed on a highly nonlinear scale. (c) Output of the two-step CDI iterative scheme.

foil and spatially filtered by means of a precision pinhole of 100 $\mu$m diameter. The diffraction pattern was detected using a charge coupled device (CCD) camera with an array of $1300\times1340$ pixels of size $\delta=20$ $\mu$m. Two sets of data were collected for each sample.

(1) The interference pattern from Young's double slits to obtain the HHG spectrum distribution $F(\lambda)$ using the maximum entropy approach.[13] The geometry of this experiment was $D=20$ $\mu$m, $W=5$ $\mu$m, and $Z=260$ mm.
(2) The diffraction pattern from the object. The sample was placed at $Z=80$ mm from the CCD.

The experimental diffraction pattern is shown in Fig. 5(b). Figure 5(c) shows the reconstructed image. Despite the low spatial resolution, $\sim1$ $\mu$m, we can clearly distinguish the main features of the object, such as a slight vertical elongation of the pinhole, and the nonuniform structure of its edges.

## V. CONCLUSION

We considered the two-step CDI approach for image reconstruction from polychromatic diffraction data. Results presented in Sec. IV demonstrate that the method is able to reconstruct images successfully from both simulated and experimental diffraction data. The approach involves the recovery of a single wavelength component from polychromatic data at a specified wavelength from the range of the spectrum of the source.

The key idea of this method is the extraction of the single monochromatic component from polychromatic diffraction data, enabling the well-established CDI technique to be applied without further modification. Since the first step of the approach involves the analysis of diffraction intensities only, which are always real and positive, the algorithm is valid for almost all types of objects, in contrast to the multiwavelength CDI approach,[12] which is limited to homogeneous objects consisting of a known material.

In summary, the possibility of using nonmonochromatic sources will evidently extend the applicability of CDI experiments to better enable the exploitation of HHG sources for diffractive imaging. Although only diffraction data produced using laser-driven HHG sources were considered here, it should be noted that the same formalism can be applied equally to any polychromatic short-wavelength source. The current activity in the development of multimode XFEL sources with high spatial resolution suggests that these approaches may find direct application in proposals to image single molecules with atomic resolution using short pulse CDI. The relaxation of the requirement that the illuminating source be strictly monochromatic in diffractive imaging technologies may well prove to be valuable in the future design and analysis of materials and biomolecules.

## ACKNOWLEDGMENTS

The work was supported by the Australian Research Council Centre of Excellence for Coherent X-ray Science.

[1] R. L. Sandberg, A. Paul, D. A. Raymondson, S. Hadrich, D. M. Gaudiosi, J. Holtsnider, R. I. Tobey, O. Cohen, M. M. Murnane, and H. C. Kapteyn, Phys. Rev. Lett. **99**, 098103 (2007).
[2] L. W. Whitehead, G. J. Williams, H. M. Quiney, K. A. Nugent, A. G. Peele, D. Paterson, M. D. de Jonge, and I. McNulty, Phys. Rev. B **77**, 104112 (2008).
[3] G. J. Williams, H. M. Quiney, A. G. Peele, and K. A. Nugent, Phys. Rev. B **75**, 104102 (2007).
[4] M. A. Pfeifer, G. J. Williams, I. A. Vartanyants, R. Harder, and I. K. Robinson, Nature (London) **442**, 63 (2006).
[5] D. Shapiro, P. Thibault, T. Beetz, V. Elser, M. Howells, Ch. Jacobsen, J. Kirz, E. Lima, H. Miao, A. M. Neiman, and D. Sayre, Proc. Natl. Acad. Sci. U.S.A. **102**, 15343 (2005).
[6] S. Marchesini, H. He, H. N. Chapman, S. P. Hau-Riege, A. Noy, M. R. Howells, U. Weiertall, and J. C. H. Spence, Phys. Rev. B **68**, 140101 (2003).
[7] J. Miao, P. Charalambous, J. Kirz, and D. Sayre, Nature (London) **400**, 342 (1999).
[8] R. W. Gerchberg and W. O. Saxton, Optik (Stuttgart) **35**, 237 (1972).
[9] J. R. Fienup, Appl. Opt. **21**, 2758 (1982).
[10] B. R. Benware, C. D. Macchietto, C. H. Moreno, and J. J. Rocca, Phys. Rev. Lett. **81**, 5804 (1998).
[11] R. A. Bartels, A. Paul, H. Green, H. C. Kapteyn, M. M. Murnane, S. Backus, I. P. Christov, Y. W. Liu, D. Attwood, and C. Jacobsen, Science **297**, 376 (2002).
[12] B. Chen, R. A. Dilanian, S. Teichmann, B. Abbey, A. G. Peele, G. J. Williams, P. Hannaford, L. V. Dao, H. M. Quiney, and K. A. Nugent, Phys. Rev. A **79**, 023809 (2009).
[13] R. A. Dilanian, B. Chen, S. Teichmann, L. V. Dao, H. M. Quiney, and K. A. Nugent, Opt. Lett. **33**, 2341 (2008).
[14] J. W. Goodman, *Introduction to Fourier Optics* (McGraw-Hill, New York, 1996).
[15] J. C. H. Spence, *Experimental High-Resolution Electron Microscopy* (Oxford University Press, New York, 1988).
[16] J. Miao, D. Sayre, and H. N. Chapman, J. Opt. Soc. Am. A Opt. Image Sci. Vis. **15**, 1662 (1998).
[17] M. Born and E. Wolf, *Principles of Optics* (Pergamon, Oxford, 1970).
[18] R. Gordon, R. Bender, and G. T. Herman, J. Theor. Biol. **29**, 471 (1970).
[19] C. H. Atkinson and J. Soria, 16th Australian Fluid Mechanics Conference, Gold Coast, Australia, 2007 (unpublished), pp. 191–198.
[20] W. Lu and F. Yin, Med. Phys. **31**, 3222 (2004).
[21] G. T. Herman and A. Lent, Comput. Biol. Med. **6**, 273 (1976).
[22] M. Nikoonahad and E. A. Ash, IEEE Ultrasonic Symposium, 1984 (unpublished), pp. 557–560.
[23] L. V. Dao, S. Teichmann, J. Davis, and P. Hannaford, J. Appl. Phys. **104**, 023105 (2008).

Downloaded 23 Oct 2009 to 136.186.1.189. Redistribution subject to AIP license or copyright; see http://jap.aip.org/jap/copyright.jsp